Article

Observation of Bose–Einstein condensation of dipolar molecules

https://doi.org/10.1038/s41586-024-07492-z

Received: 18 December 2023

Accepted: 30 April 2024

Published online: 3 June 2024

Check for updates

Niccolò Bigagli[1,3], Weijun Yuan[1,3], Siwei Zhang[1,3], Boris Bulatovic[1], Tijs Karman[2], Ian Stevenson[1] & Sebastian Will[1]✉

Ensembles of particles governed by quantum mechanical laws exhibit intriguing emergent behaviour. Atomic quantum gases[1,2], liquid helium[3,4] and electrons in quantum materials[5–7] all exhibit distinct properties because of their composition and interactions. Quantum degenerate samples of ultracold dipolar molecules promise the realization of new phases of matter and new avenues for quantum simulation[8] and quantum computation[9]. However, rapid losses[10], even when reduced through collisional shielding techniques[11–13], have so far prevented evaporative cooling to a Bose–Einstein condensate (BEC). Here we report on the realization of a BEC of dipolar molecules. By strongly suppressing two- and three-body losses via enhanced collisional shielding, we evaporatively cool sodium–caesium molecules to quantum degeneracy and cross the phase transition to a BEC. The BEC reveals itself by a bimodal distribution when the phase-space density exceeds 1. BECs with a condensate fraction of 60(10)% and a temperature of 6(2) nK are created and found to be stable with a lifetime close to 2 s. This work opens the door to the exploration of dipolar quantum matter in regimes that have been inaccessible so far, promising the creation of exotic dipolar droplets[14], self-organized crystal phases[15] and dipolar spin liquids in optical lattices[16].

The behaviour of many-body quantum systems is dictated by the interactions between their constituents. Starting from weak contact interactions, Bose–Einstein condensates (BECs) of neutral atoms[1,2] were instrumental in gaining full control over atoms and in understanding basic properties of superfluids. In conjunction with the ability to tune the strength of contact interactions[17,18], BECs established quantum simulation as a viable experimental method[19,20]. BECs of highly magnetic atoms enabled the study of systems with weak long-range dipole–dipole interactions[21] and the realization of rich phases of matter such as quantum ferrofluids[22], droplets[23,24] and supersolids[25–27]. Even stronger interactions give rise to the intriguing properties of liquid helium[28] or electron gases in solid-state systems[29,30].

Quantum gases of ground state dipolar molecules have been proposed as a clean and controlled system in which long-range interactions can be tuned from the weakly interacting to the strongly interacting regime. Similar to dilute atomic clouds, in the limit of weak interactions bosonic molecules are expected to show a phase transition to a BEC. Once the strength of interactions is increased, theoretical predictions abound both for bosonic and fermionic molecules[31] and include the realization of strongly correlated phases of matter[14], from supersolids[32] to dipolar crystals[15] and Mott insulators with fractional filling[33]. Thus, low-entropy samples of dipolar molecules with tunable interactions promise to constitute a platform for many-body physics and quantum simulation.

The realization of a BEC of dipolar molecules has remained elusive for more than two decades, since the first theoretical ideas on their use were explored[9,33]. In 2008, the first ultracold gases of dipolar molecules were created by association from ultracold atoms[34]. Soon it was found that chemical reactions can lead to fast losses that limited their lifetimes[10]. In hopes to mitigate these losses, ground state samples of chemically stable species[35] were prepared[36–38], but the problem of short lifetimes remained[39–41]. Exploiting favourable quantum statistics, it was shown that degenerate molecular Fermi gases can be directly created by associating molecules from quantum degenerate atomic samples[42,43]. Recently, various collisional shielding techniques[44–47] have led to the production of molecular clouds with reduced losses, which was sufficient to create quantum degenerate gases of fermionic molecules by evaporative cooling[11,48]. However, for bosonic molecules, losses are intrinsically higher because of quantum statistical bunching[49], and recent work[50,51] showed that further substantial improvements to collisional shielding are required to realize the phase transition from a thermal gas to a BEC.

Here we demonstrate the realization of a BEC of dipolar molecules. By strongly suppressing two- and three-body losses, we evaporatively cool ensembles of sodium–caesium (NaCs) molecules from 700(50) nK to 6(2) nK within 3 s. Figure 1a,b shows sample images during the evaporation sequence and an illustration of the experimental approach. We reach the critical phase-space density for a BEC with more than 2,000 molecules and further evaporate to BECs with 200 molecules and small thermal fractions. The BECs are found to be stable, with a $1/e$ lifetime of 1.8(1) s. These results show how molecules have achieved a degree of quantum control analogous to that of atoms, markedly expanding the scope of the quantum systems that can be studied.

[1]Department of Physics, Columbia University, New York, NY, USA. [2]Institute for Molecules and Materials, Radboud University, Nijmegen, The Netherlands. [3]These authors contributed equally: Niccolò Bigagli, Weijun Yuan, Siwei Zhang. ✉e-mail: sebastian.will@columbia.edu

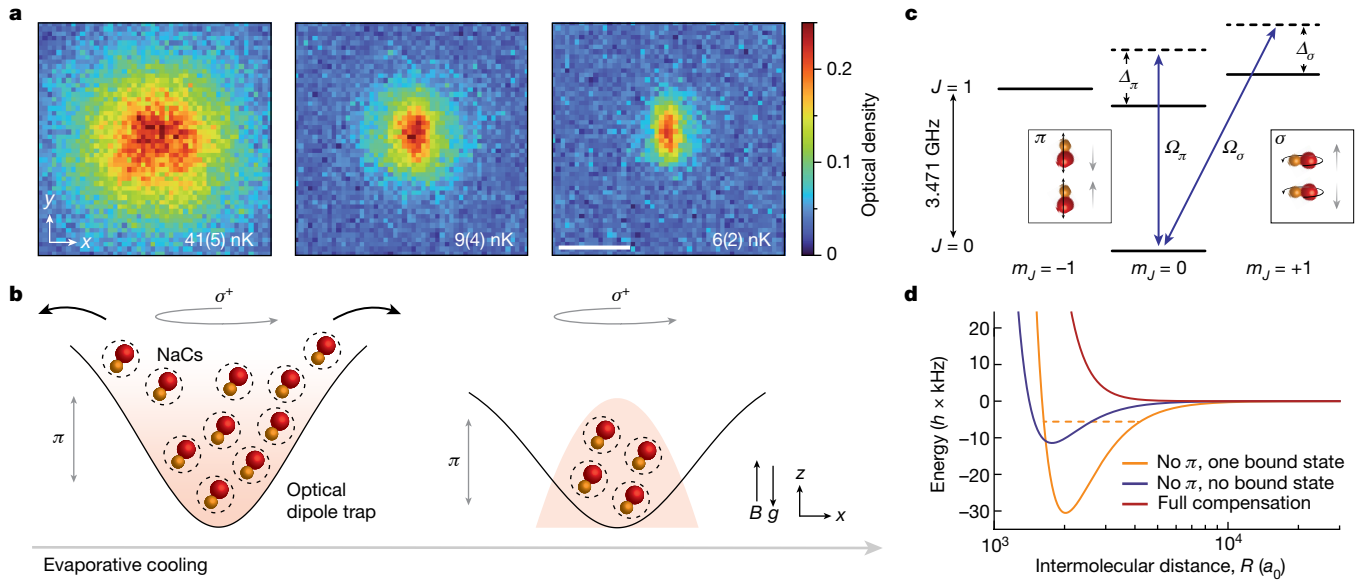

Fig. 1 | BEC of dipolar NaCs molecules enabled by microwave shielding. **a**, Absorption images of a thermal cloud (left), a partially condensed cloud (middle) and a quasi-pure BEC (right) after 17 ms of time-of-flight expansion. Each image is an average of 20 individual pictures. The clouds, from left to right, correspond to those labelled 1, 3 and 5 in Figs. 2 and 3a. **b**, Evaporative cooling of NaCs molecules from a thermal cloud to a BEC. The molecules are held in an optical dipole trap and dressed by circularly polarized (σ^+) and linearly polarized (π) microwave fields. The collisionally stable molecular gas is cooled by lowering the trap depth, forcing out the hottest molecules. Thermal (left) and condensed (right) gases have different density profiles. **c**, Rotational levels of NaCs, coherently coupled by two microwave fields. The shielded dressed state is a superposition of $|J, m_J\rangle = |0, 0\rangle$, $|1, 0\rangle$ and $|1, 1\rangle$. The σ^+ microwave field has a Rabi frequency Ω_σ and a detuning Δ_σ from the $|0, 0\rangle \leftrightarrow |1, 1\rangle$ transition, and the π microwave field has a Rabi frequency Ω_π and a detuning Δ_π from the $|0, 0\rangle \leftrightarrow |1, 0\rangle$ transition. The boxes show the compensation of the π- and σ^+-induced dipole moments for a collision of two molecules in the vertical direction: the vertically oscillating dipole moments, induced by the π field, interact attractively; conversely, the rotating dipole moments, induced by the σ^+ field, interact repulsively. **d**, Potential energy curves of microwave-shielded molecules approaching in the s-wave channel. The Rabi frequencies and detunings are: for the red line $\Omega_\sigma = 2\pi \times 7.9$ MHz, $\Delta_\sigma = 2\pi \times 8$ MHz and $\Omega_\pi = 2\pi \times 6.5$ MHz, $\Delta_\pi = 2\pi \times 10$ MHz; for the orange line $\Omega_\sigma = 2\pi \times 7.9$ MHz, $\Delta_\sigma = 2\pi \times 8$ MHz and no π field; and for the blue line $\Omega_\sigma = 2\pi \times 7.9$ MHz, $\Delta_\sigma = 2\pi \times 17$ MHz and no π field. The experimental uncertainty of Ω_σ is 0.3 MHz and that of Ω_π is 0.2 MHz. Scale bar, 20 μm (**a**).

Microwave shielding

For efficient evaporative cooling, collisional losses need to be strongly suppressed. To achieve this, we transfer the molecules into a dressed state using two different microwave fields, one with circular σ^+ polarization and one with linear π polarization. The level diagram for the bare rotational states of NaCs and the microwave frequencies coupling them is shown in Fig. 1c.

Microwave shielding, as demonstrated so far, has a fundamental limit to its effectiveness as there is a trade-off between the suppression of two- and three-body losses[50]. Our current understanding is as follows: when a single circularly polarized microwave field is used, a superposition of two rotational states induces a rotating dipole moment. At short range, this forms a strong repulsive barrier that prevents two-body loss; the stronger the microwave coupling, the lower the losses. At long range, the dipole–dipole interactions remain attractive (in the s-wave channel). As a result, at an intermolecular distance of about 2,000 a_0 (a_0 denotes the Bohr radius), an attractive potential well appears (Fig. 1d) that supports field-linked bound states when the microwave coupling is strong[52,53]. These bound states can give rise to loss by three-body recombination, hence the more effective the suppression of two-body loss, the stronger the three-body losses. This sets a lower limit to the achievable loss rates and subsequently caps the efficiency of evaporative cooling. The blue and orange curves in Fig. 1d show the intermolecular potentials for shielding with a far-detuned and a near-detuned σ^+ field, limited by two- and three-body losses, respectively.

To suppress three-body losses, the field-linked bound states need to be removed while preserving a highly effective suppression of two-body loss. This is achieved by compensating for the attractive dipole–dipole interactions at long range while leaving the dipole-induced repulsive barrier at short range unaffected. Dipole–dipole interactions of rotating dipoles induced by a σ^+ field and oscillating dipoles induced by a π field have opposite signs[47]. By simultaneously dressing the molecules with a circularly and a linearly polarized microwave field, we compensate for the induced dipole–dipole interactions and minimize the long-range attraction (T.K. et al., manuscript in preparation). This enables the engineering of a purely repulsive intermolecular potential, shown as the red curve in Fig. 1d, minimizing both two- and three-body losses. A similar compensation of the induced dipole moment can also be achieved by combining the microwave and electrostatic fields[54,55].

In addition to suppressing collisional losses, our microwave dressing scheme helps tuning the molecular interactions to a regime in which Bose–Einstein condensation is possible. In the case of bosonic dipolar molecules, the interactions are composed of s-wave contact interactions, characterized by the s-wave scattering length, a_s, and dipole–dipole interactions, characterized by the dipolar length, $a_{dd} = Md_{eff}^2/(12\pi\hbar^2\epsilon_0)$, where M denotes the mass of NaCs, d_{eff} the effective dipole moment, $\hbar$ the Planck constant h divided by 2π and ϵ_0 the permittivity of free space. For stable BECs of dipolar particles, the interactions must be repulsive ($a_s > 0$), weak ($n_0 a_s^3 \ll 1$ and $n_0 a_{dd}^3 \ll 1$, where n_0 is the peak number density), and the dipolar interactions should be weaker than or of the order of contact interactions ($\epsilon_{dd} \equiv a_{dd}/a_s \lesssim 1$) (ref. 21). For NaCs molecules dressed by a single σ^+ field that is sufficiently strong to suppress two-body loss, a_{dd} is between approximately 10,000 a_0 and 25,000 a_0, making it hard to fulfil these conditions. With the presence of the π field, the dipolar length can be strongly reduced. Although in principle the full cancellation of dipolar interactions is possible, in practice we achieve $a_{dd} \approx 1{,}300\ a_0$, because of the finite ellipticity of the σ^+ field, and $a_s \approx 1{,}500\ a_0$. Full details on the calculation of a_s and a_{dd} are reported in a recent study

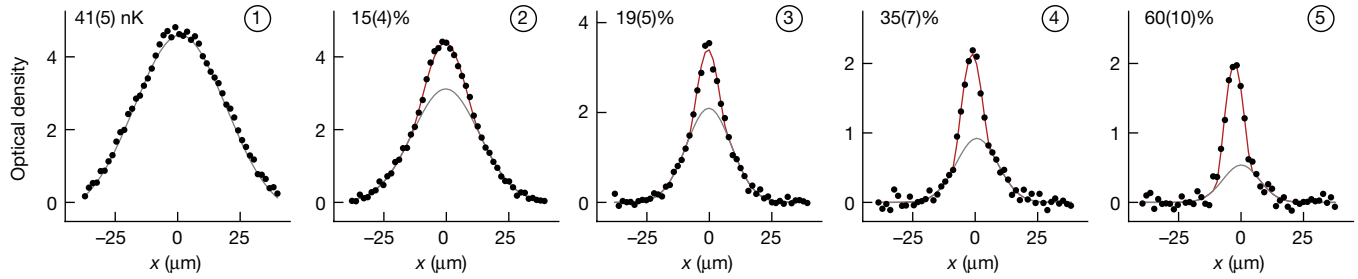

Fig. 2 | Formation of the molecular BEC. Each plot shows the 1D profile of absorption images (integrated along the *y* axis) at different stages of the evaporative cooling sequence, going from a thermal distribution to bimodal distributions to a highly condensed gas (left to right). The red lines show bimodal Thomas–Fermi plus Gaussian fits to the profiles; the grey lines separately show the Gaussian part of the fit. On the top-left corner, the temperature (for the thermal cloud) and the condensate fraction (for the partially condensed clouds; see Methods) are shown. The temperature is obtained from ballistic expansion. Each plot shows an average of 20 images after 17 ms time-of-flight expansion. The encircled numbers indicate the corresponding data points in Fig. 3a.

(T.K. et al., manuscript in preparation). Conversely, we believe that the flexible control of a_{dd} by dressing fields will be a cornerstone to gaining access to strongly interacting dipolar phases with $\epsilon_{dd} > 1$ (refs. 14,15) in future work.

Evaporative cooling

Our experiment begins with gases of 30,000 NaCs molecules in their electronic, vibrational and rotational ground states, held in a crossed optical dipole trap at a temperature of 700(50) nK. The molecules are adiabatically prepared in the collisionally shielded dressed state by sequentially ramping up a circularly polarized σ^+ and a linearly polarized π microwave field. We found $\Omega_\sigma = 2\pi \times 7.9(0.3)$ MHz, $\Delta_\sigma = 2\pi \times 8$ MHz, $\Omega_\pi = 2\pi \times 6.5(0.2)$ MHz and $\Delta_\pi = 2\pi \times 10$ MHz to provide good working conditions for evaporative cooling. Here, Ω_σ and Δ_σ are the Rabi frequency and detuning of the σ^+ field and Ω_π and Δ_π are the Rabi frequency and detuning of the π field. Details on the preparation of the sample and on the generation of the microwave fields are provided in the Methods.

We perform forced evaporation by decreasing the depth of the optical dipole trap from $k_B \times 5.3(0.3)$ μK to $k_B \times 40(15)$ nK within 2.8 s, followed by free evaporation for 400 ms by holding the sample in the low-depth trap (Fig. 3a, inset). During the evaporation sequence, the trap frequencies decrease from $\omega/(2\pi) = (45, 78, 162)$ Hz to $\omega/(2\pi) = (23, 49, 58)$ Hz. We record absorption images of the molecular cloud after time-of-flight expansion at various points of the cooling sequence, as shown in Fig. 2. Close to the end of the cooling sequence, we start to observe the formation of a BEC through the emergence of a bimodal density distribution. Analysing the density profiles of the molecular clouds, we find that a bimodal fit captures the shape notably better than a purely Gaussian fit, as shown in Extended Data Fig. 2. For larger condensate fractions, we observe a marked offset along the *x* axis between the centre of the thermal and condensed components, potentially caused by trap imperfections or repulsion between the two components in time of flight. At the end of the cooling sequence, we observe a BEC with a small thermal cloud surrounding it.

Molecular BEC

To analyse the cooling process, we determine the phase-space density (PSD), temperature and peak density of the thermal molecular gas at various points of the cooling sequence (Fig. 3). Their evolution is plotted as a function of molecule number in Fig. 3a–c. Our sample starts at a PSD of 5×10^{-3} and the BEC transition is expected at a PSD of 1.202 in a 3D harmonic trap. We reach a PSD of about 1 at 20 nK with more than 2,000 molecules. This aligns with the point at which the density profiles show the onset of a bimodal distribution in time of flight with a condensed core and a thermal cloud surrounding it. Beyond this point, instead of PSD, we plot the condensate fraction,

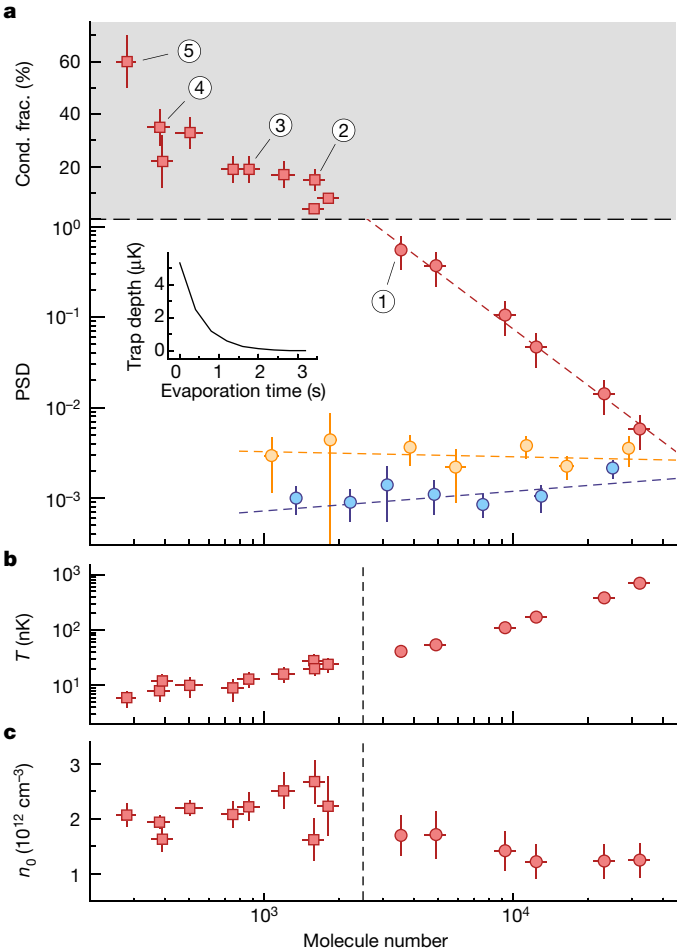

Fig. 3 | Evaporative cooling of NaCs molecules to quantum degeneracy. **a**, The evolution of the PSD and condensate fraction of the microwave-shielded molecular gas with a purely repulsive intermolecular potential is shown in red. Evaporation attempts of molecular gases with σ^+-only shielding are shown in orange and blue. The respective microwave parameters correspond to the data with the same colour in Fig. 1d. The dashed lines are power-law fits to the PSD of the thermal clouds used to extract the evaporation efficiency. Error bars show the standard error of the mean of two runs of the experiment. Inset, the time evolution of the trap depth during the evaporation sequence. **b**, Decrease of temperature during evaporation. In the thermal regime, temperatures are obtained from time-of-flight expansion of the thermal gas. In the degenerate regime, temperatures are obtained from the expansion of the thermal component of the cloud. **c**, Evolution of peak density during the evaporation. In **b** and **c**, the vertical dashed lines mark the onset of condensation. For all data points in the figure, circles denote data for thermal clouds and squares denote data for degenerate clouds. Cond. frac., condensate fraction.

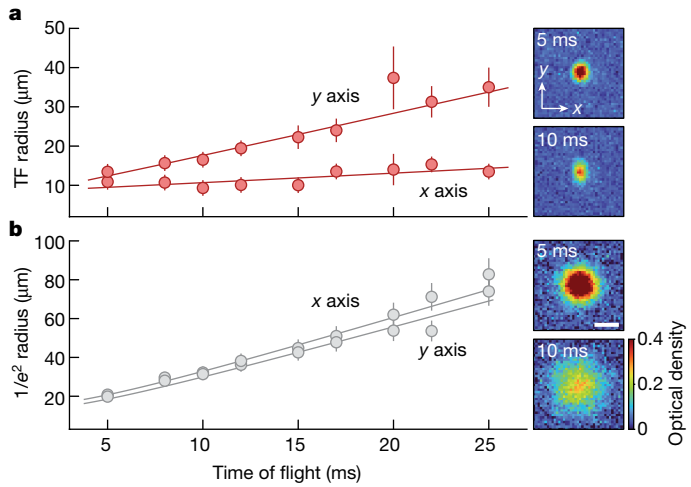

Fig. 4 | Time-of-flight expansion. a, Quasi-pure BEC with a condensate fraction of more than 50% released from an elongated trap with trap frequencies $\omega_x/(2\pi) = 23(2)$ Hz and $\omega_y/(2\pi) = 49(3)$ Hz. The solid lines are linear fits to the radii. **b**, Thermal gas at $T = 37(4)$ nK, just before the onset of degeneracy, released from an elongated trap with trap frequencies $\omega_x/(2\pi) = 23(2)$ Hz and $\omega_y/(2\pi) = 53(3)$ Hz. The solid lines are fits to the expansion of the thermal cloud that enable us to retrieve its temperature. For the BEC (thermal gas), data points show the Thomas–Fermi radius (Gaussian $1/e^2$ radius) for both the x and y axes. Each data point is the average of 20(5) iterations of the experiment. Error bars show the 1σ uncertainty from the fits. Scale bar, 25 μm.

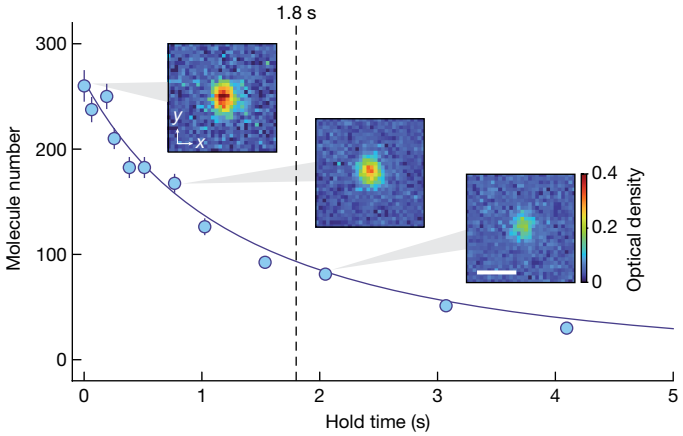

Fig. 5 | BEC lifetime. The BEC is held in the optical dipole trap for a variable hold time and the molecule number is recorded. The initial peak density is $n_0 = 2.0(5) \times 10^{12}$ cm^{-3}. Each data point before 1 s is the average of 5 images and after 1 s is the average of 10 images. The insets are averaged images at different hold times, recorded after 8 ms of time of flight. Errors show the standard error of the mean from 3 runs of the experiment. Scale bar, 25 μm.

that is, the ratio of the number of molecules in the condensed core and the total number of molecules in the gas, as extracted from bimodal fits. At the end of evaporation, we observe a condensate fraction of 60(10)% for our coldest clouds. From fits to the expansion of the thermal wings, we obtain a temperature of 6(2) nK. Using the data points in the thermal regime, we also determine the evaporation efficiency to be $-d\ln(\mathrm{PSD})/d\ln(N) = 2.0(1)$. In the course of the evaporative cooling sequence, the PSD increases by more than three orders of magnitude, which far exceeds the gains observed in previous demonstrations of evaporative cooling of molecules[11,48,56,57].

The peak density of the molecular cloud stays approximately constant during the evaporation (Fig. 3c). In the thermal regime, it is around $n_0 = 1.5(3) \times 10^{12}$ cm^{-3}, before slightly increasing to $n_0 = 2.0(5) \times 10^{12}$ cm^{-3} in the degenerate regime (Methods). Compared with atomic BECs, which often reach peak densities above 10^{14} cm^{-3}, these are unusually low densities, induced by the large value of a_s. Owing to these conditions, our system is in the weakly interacting regime $n_0 a_s^3 \ll 1$ and $n_0 a_{dd}^3 \ll 1$, which ensures that quantum depletion is negligible.

To illustrate the efficacy of the enhanced microwave shielding scheme used in this work, we also show the evolution of PSD for two cases of σ^+-only shielding. These two cases correspond to the scattering potentials shown in Fig. 1d. Following the exact same evaporation ramp of the optical dipole trap as with the enhanced shielding scheme, we now observe an evaporation efficiency of −0.2(1) for the scattering potential with a weaker collisional barrier (blue) and 0.1(1) for the scattering potential with a stronger collisional barrier and larger long-range attraction (orange). These shielding schemes come with significantly higher loss rates, such that no significant gains in PSD are made for the given sequence.

Condensate properties

Having established the phase transition to a BEC, we investigate some of its qualitative properties. First, we observe the expansion dynamics in free flight by releasing a quasi-pure BEC from an elongated trap with aspect ratio $\omega_x/\omega_y \approx 0.5$. We observe an anisotropic expansion of the condensate and the inversion of aspect ratio (Fig. 4a). This aligns with the expected behaviour of matter wave-type expansion of a BEC released from an elongated trap[58]. It is markedly different from the behaviour of a thermal cloud that typically expands isotropically, independent of the aspect ratio of the trap. We confirm that a thermal molecular gas just before the onset of condensation expands isotropically when released from a trap with the same aspect ratio, as shown in Fig. 4b. In how far the residual dipolar interactions affect the dynamics of the expanding BEC is a question that will be addressed in future work by studying the expansion dynamics as a function of the magnitude and direction of the dipole moment that can be controlled by the microwave dressing fields. We also note that the observation of an expanding BEC provides further confirmation that a weakly dipolar gas has been created in contrast, for example, to a self-bound droplet that would not expand in time of flight[24].

Second, we measure the BEC lifetime. As shown in Fig. 5, we observe the molecule number in the BEC as a function of hold time in an optical dipole trap with a depth of $k_B \times 40(15)$ nK. As three-body processes are strongly suppressed because of enhanced microwave shielding, we fit the data with a kinetic model that includes one- and two-body losses specific to a BEC (Methods). We find a $1/e$ lifetime of the condensate of 1.8(1) s. The condensate fraction seems to be constant throughout the measurement. From the data, we also extract a two-body loss rate of $\beta_{2B} = 3(1) \times 10^{-13}$ cm^3 s^{-1}, which arises from the combined effect of residual collisional losses and free evaporation in the relatively shallow trap. This loss rate is four orders of magnitude lower than the loss rate of unshielded molecules.

Conclusion

In conclusion, we have created a BEC of dipolar molecules. Leveraging the tunability of dipolar interactions, we achieved a dramatic suppression of losses and simultaneously created the conditions for a weakly interacting Bose gas. With hundreds of molecules in an identical internal and motional state, the BEC is an ideal starting point for the exploration of strongly dipolar quantum matter. Owing to its large dipole moment of 4.75 D (ref. 59), NaCs is ideally suited to tune between the weakly and strongly dipolar regimes, which is hard to achieve in other dipolar systems, such as magnetic atoms or Rydberg atoms. The next important frontier will be to explore experimental pathways to turn the weakly interacting Bose gas into a strongly interacting system. Although control over the two microwave dressing fields will readily allow the increase of dipolar interaction strength, it is a

key open question in how far effective collisional shielding can be simultaneously maintained.

With the ability to create stable BECs, dipolar molecules make a marked leap towards becoming a new modality for quantum simulation, quantum information and the exploration of many-body quantum systems. The BEC should give direct access to exotic forms of self-organization in 3D, such as the formation of droplet arrays[23] and macrodroplets[24], predicted for densities and interaction strengths that can be reached from current conditions. In 2D systems, the emergence of strongly interacting superfluids, dipolar crystals, supersolid and hexatic phases has been predicted[15,31]. Furthermore, the BEC should be an ideal starting point for the study of optical lattice systems with dipolar molecules. Stabilized through microwave shielding, the realization of extended Hubbard models with finite tunnelling and wide tunability of interactions comes within reach, giving access to Mott insulators with fractional filling[60]. In particular, it should become possible to realize the long-standing goal of loading optical lattices with unity filling, that is, exactly one molecule per lattice site. This will be an important prerequisite for the realization of spin models with hundreds of interacting spins[61]. Combining the lattice-loaded molecules with microwave dressing schemes, the formation of topologically ordered phases[62] or dipolar spin liquids[16,63] may also come within reach.

Online content

Any methods, additional references, Nature Portfolio reporting summaries, source data, extended data, supplementary information, acknowledgements, peer review information; details of author contributions and competing interests; and statements of data and code availability are available at https://doi.org/10.1038/s41586-024-07492-z.

1. Anderson, M. H., Ensher, J. R., Matthews, M. R., Wieman, C. E. & Cornell, E. A. Observation of Bose-Einstein condensation in a dilute atomic vapor. *Science* **269**, 198–201 (1995).
2. Davis, K. B. et al. Bose-Einstein condensation in a gas of sodium atoms. *Phys. Rev. Lett.* **75**, 3969–3973 (1995).
3. Kapitza, P. Viscosity of liquid helium below the λ-point. *Nature* **141**, 74 (1938).
4. Allen, J. F. & Misener, A. Flow of liquid helium II. *Nature* **141**, 75 (1938).
5. Tsui, D. C., Stormer, H. L. & Gossard, A. C. Two-dimensional magnetotransport in the extreme quantum limit. *Phys. Rev. Lett.* **48**, 1559–1562 (1982).
6. Bednorz, J. G. & Müller, K. A. Possible high T_c superconductivity in the Ba–La–Cu–O system. *Z. Phys. B Condens. Matter* **64**, 189–193 (1986).
7. Cao, Y. et al. Unconventional superconductivity in magic-angle graphene superlattices. *Nature* **556**, 43–50 (2018).
8. Micheli, A., Brennen, G. & Zoller, P. A toolbox for lattice-spin models with polar molecules. *Nat. Phys.* **2**, 341–347 (2006).
9. DeMille, D. Quantum computation with trapped polar molecules. *Phys. Rev. Lett.* **88**, 067901 (2002).
10. Ospelkaus, S. et al. Quantum-state controlled chemical reactions of ultracold potassium-rubidium molecules. *Science* **327**, 853–857 (2010).
11. Valtolina, G. et al. Dipolar evaporation of reactive molecules to below the Fermi temperature. *Nature* **588**, 239–243 (2020).
12. Matsuda, K. et al. Resonant collisional shielding of reactive molecules using electric fields. *Science* **370**, 1324–1327 (2020).
13. Anderegg, L. et al. Observation of microwave shielding of ultracold molecules. *Science* **373**, 779–782 (2021).
14. Schmidt, M., Lassablière, L., Quéméner, G. & Langen, T. Self-bound dipolar droplets and supersolids in molecular Bose-Einstein condensates. *Phys. Rev. Res.* **4**, 013235 (2022).
15. Büchler, H. P. et al. Strongly correlated 2D quantum phases with cold polar molecules: controlling the shape of the interaction potential. *Phys. Rev. Lett.* **98**, 060404 (2007).
16. Yao, N. Y., Zaletel, M. P., Stamper-Kurn, D. M. & Vishwanath, A. A quantum dipolar spin liquid. *Nat. Phys.* **14**, 405–410 (2018).
17. Inouye, S. et al. Observation of feshbach resonances in a bose–einstein condensate. *Nature* **392**, 151–154 (1998).
18. Greiner, M., Mandel, O., Esslinger, T., Hänsch, T. W. & Bloch, I. Quantum phase transition from a superfluid to a Mott insulator in a gas of ultracold atoms. *Nature* **415**, 39–44 (2002).
19. Zwerger, W. *The BCS-BEC Crossover and the Unitary Fermi Gas* Lecture Notes in Physics, Vol. 836 (Springer Science & Business Media, 2011).
20. Gross, C. & Bloch, I. Quantum simulations with ultracold atoms in optical lattices. *Science* **357**, 995–1001 (2017).
21. Chomaz, L. et al. Dipolar physics: a review of experiments with magnetic quantum gases. *Rep. Prog. Phys.* **86**, 026401 (2022).
22. Lahaye, T. et al. Strong dipolar effects in a quantum ferrofluid. *Nature* **448**, 672–675 (2007).
23. Kadau, H. et al. Observing the Rosensweig instability of a quantum ferrofluid. *Nature* **530**, 194–197 (2016).
24. Chomaz, L. et al. Quantum-fluctuation-driven crossover from a dilute Bose-Einstein condensate to a macrodroplet in a dipolar quantum fluid. *Phys. Rev. X* **6**, 041039 (2016).
25. Böttcher, F. et al. Transient supersolid properties in an array of dipolar quantum droplets. *Phys. Rev. X* **9**, 011051 (2019).
26. Chomaz, L. et al. Long-lived and transient supersolid behaviors in dipolar quantum gases. *Phys. Rev. X* **9**, 021012 (2019).
27. Tanzi, L. et al. Observation of a dipolar quantum gas with metastable supersolid properties. *Phys. Rev. Lett.* **122**, 130405 (2019).
28. Wilks, J. *The Properties of Liquid and Solid Helium* (Clarendon, 1967).
29. Bardeen, J., Cooper, L. N. & Schrieffer, J. R. Theory of superconductivity. *Phys. Rev.* **108**, 1175–1204 (1957).
30. Laughlin, R. B. Anomalous quantum hall effect: an incompressible quantum fluid with fractionally charged excitations. *Phys. Rev. Lett.* **50**, 1395–1398 (1983).
31. Baranov, M. A., Dalmonte, M., Pupillo, G. & Zoller, P. Condensed matter theory of dipolar quantum gases. *Chem. Rev.* **112**, 5012–5061 (2012).
32. Pollet, L., Picon, J., Büchler, H. & Troyer, M. Supersolid phase with cold polar molecules on a triangular lattice. *Phys. Rev. Lett.* **104**, 125302 (2010).
33. Góral, K., Santos, L. & Lewenstein, M. Quantum phases of dipolar bosons in optical lattices. *Phys. Rev. Lett.* **88**, 170406 (2002).
34. Ni, K.-K. et al. A high phase-space-density gas of polar molecules. *Science* **322**, 231–235 (2008).
35. Żuchowski, P. S. & Hutson, J. M. Reactions of ultracold alkali-metal dimers. *Phys. Rev. A* **81**, 060703 (2010).
36. Takekoshi, T. et al. Ultracold dense samples of dipolar RbCs molecules in the rovibrational and hyperfine ground state. *Phys. Rev. Lett.* **113**, 205301 (2014).
37. Molony, P. K. et al. Creation of ultracold $^{87}Rb^{133}Cs$ molecules in the rovibrational ground state. *Phys. Rev. Lett.* **113**, 255301 (2014).
38. Park, J. W., Will, S. A. & Zwierlein, M. W. Ultracold dipolar gas of fermionic $^{23}Na^{40}K$ molecules in their absolute ground state. *Phys. Rev. Lett.* **114**, 205302 (2015).
39. Ye, X., Guo, M., González-Martínez, M. L., Quéméner, G. & Wang, D. Collisions of ultracold $^{23}Na^{87}Rb$ molecules with controlled chemical reactivities. *Sci. Adv.* **4**, eaaq0083 (2018).
40. Gregory, P. D. et al. Sticky collisions of ultracold RbCs molecules. *Nat. Commun.* **10**, 3104 (2019).
41. Bause, R. et al. Collisions of ultracold molecules in bright and dark optical dipole traps. *Phys. Rev. Res.* **3**, 033013 (2021).
42. De Marco, L. et al. A degenerate fermi gas of polar molecules. *Science* **363**, 853–856 (2019).
43. Duda, M. et al. Transition from a polaronic condensate to a degenerate fermi gas of heteronuclear molecules. *Nat. Phys.* **19**, 720–725 (2023).
44. Cooper, N. & Shlyapnikov, G. V. Stable topological superfluid phase of ultracold polar fermionic molecules. *Phys. Rev. Lett.* **103**, 155302 (2009).
45. Micheli, A. et al. Universal rates for reactive ultracold polar molecules in reduced dimensions. *Phys. Rev. Lett.* **105**, 073202 (2010).
46. Lassablière, L. & Quéméner, G. Controlling the scattering length of ultracold dipolar molecules. *Phys. Rev. Lett.* **121**, 163402 (2018).
47. Karman, T. & Hutson, J. M. Microwave shielding of ultracold polar molecules. *Phys. Rev. Lett.* **121**, 163401 (2018).
48. Schindewolf, A. et al. Evaporation of microwave-shielded polar molecules to quantum degeneracy. *Nature* **607**, 677–681 (2022).
49. Julienne, P. S., Hanna, T. M. & Idziaszek, Z. Universal ultracold collision rates for polar molecules of two alkali-metal atoms. *Phys. Chem. Chem. Phys.* **13**, 19114–19124 (2011).
50. Bigagli, N. et al. Collisionally stable gas of bosonic dipolar ground-state molecules. *Nat. Phys.* **19**, 1579–1584 (2023).
51. Lin, J. et al. Microwave shielding of bosonic NaRb molecules. *Phys. Rev. X* **13**, 031032 (2023).
52. Avdeenkov, A. & Bohn, J. L. Linking ultracold polar molecules. *Phys. Rev. Lett.* **90**, 043006 (2003).
53. Chen, X.-Y. et al. Ultracold field-linked tetratomic molecules. *Nature* **626**, 283–287 (2024).
54. Micheli, A., Pupillo, G., Büchler, H. & Zoller, P. Cold polar molecules in two-dimensional traps: tailoring interactions with external fields for novel quantum phases. *Phys. Rev. A* **76**, 043604 (2007).
55. Gorshkov, A. V. et al. Suppression of inelastic collisions between polar molecules with a repulsive shield. *Phys. Rev. Lett.* **101**, 073201 (2008).
56. Son, H., Park, J. J., Ketterle, W. & Jamison, A. O. Collisional cooling of ultracold molecules. *Nature* **580**, 197–200 (2020).
57. Li, J.-R. et al. Tuning of dipolar interactions and evaporative cooling in a three-dimensional molecular quantum gas. *Nat. Phys.* **17**, 1144–1148 (2021).
58. Mewes, M.-O. et al. Bose-Einstein condensation in a tightly confining dc magnetic trap. *Phys. Rev. Lett.* **77**, 416–419 (1996).
59. Dagdigian, P. J. & Wharton, L. Molecular beam electric deflection and resonance spectroscopy of the heteronuclear alkali dimers: $^{39}K^7Li$, Rb^7Li, $^{39}K^{23}Na$, $Rb^{23}Na$, and $^{133}Cs^{23}Na$. *J. Chem. Phys.* **57**, 1487–1496 (1972).
60. Capogrosso-Sansone, B., Trefzger, C., Lewenstein, M., Zoller, P. & Pupillo, G. Quantum phases of cold polar molecules in 2D optical lattices. *Phys. Rev. Lett.* **104**, 125301 (2010).
61. Gorshkov, A. V. et al. Tunable superfluidity and quantum magnetism with ultracold polar molecules. *Phys. Rev. Lett.* **107**, 115301 (2011).
62. Manmana, S. R., Stoudenmire, E., Hazzard, K. R., Rey, A. M. & Gorshkov, A. V. Topological phases in ultracold polar-molecule quantum magnets. *Phys. Rev. B* **87**, 081106 (2013).
63. Büchler, H., Micheli, A. & Zoller, P. Three-body interactions with cold polar molecules. *Nat. Phys.* **3**, 726–731 (2007).

Methods

Sample preparation and detection

The starting point for the experiments in this work are ensembles with about 30,000 ground state NaCs molecules at a temperature of 700(50) nK. At the beginning of forced evaporation, the sample is held in a crossed optical dipole trap with trap frequencies $\omega/(2\pi) = (45, 78, 162)$ Hz (measured for NaCs ground state molecules). The *x*-dipole trap is elliptical and focused to waists of 108(1) μm (horizontal) and 51.5(5) μm (vertical); the *y*-dipole trap is almost circular with waists of 117(1) μm (horizontal) and 104.5(5) μm (vertical). Optical trapping light is generated by a 1,064-nm narrow-line single-mode Nd:YAG laser (Coherent Mephisto MOPA). At the end of evaporation, the trap frequencies are $\omega/(2\pi) = (23, 49, 58)$ Hz.

The ensembles of ground state molecules are prepared in three steps. First, overlapping ultracold gases of Na and Cs atoms are created[64]. Second, weakly bound NaCs Feshbach molecules are assembled by a magnetic field ramp across the Feshbach resonance at $B_{res} = 864.1(1)$ G (ref. 65). The magnetic field points in *z*-direction and sets the quantization axis. Third, NaCs Feshbach molecules are transferred to the electronic, vibrational and rotational ground state, $X^1\Sigma^+|v, J\rangle = |0, 0\rangle$, using stimulated Raman adiabatic passage (STIRAP)[66,67]. The specific hyperfine state of ground state molecules is $|m_{I_{Na}}, m_{I_{Cs}}\rangle = |3/2, 5/2\rangle$, where $m_{I_{Na}}$ is the projection of the nuclear spin of sodium and $m_{I_{Cs}}$ is the projection of the nuclear spin of caesium onto the quantization axis. Owing to the large *B* field, the nuclear spin is decoupled from the rotational spin, such that the hyperfine substructure does not need to be considered in the microwave shielding process. The STIRAP beams propagate vertically along the *z* axis, parallel to gravity. In this way, the molecules remain inside the STIRAP beam profiles as they fall and expand in time of flight while shielded in the ground state to prevent losses. This is important for precise thermometry of the molecular gas[50].

At the end of time-of-flight expansion, the NaCs molecules are detected by ramping down the dressing fields (80 μs), performing bound-to-free reverse STIRAP resulting in Cs atoms in $|F, m_F\rangle = |3, 3\rangle$ (20 μs, 75(3)% efficiency), and optically pumping with a laser pulse (100 μs) that is resonant with the Cs $6^2S_{1/2}|3, 3\rangle \rightarrow 6^2P_{3/2}|4, 4\rangle$ transition at high magnetic field that depletes the initial state, immediately followed by absorption imaging of Cs atoms with a laser pulse (100 μs) that is resonant with the Cs $6^2S_{1/2}|4, 4\rangle \rightarrow 6^2P_{3/2}|5, 5\rangle$ transition at high magnetic field. Here *F* is the total atomic angular momentum and m_F its projection onto the quantization axis. We correct the molecule numbers for the STIRAP efficiency and neglect the imperfections in optical pumping (about 10%). The imaging resolution in our system is 4.5(5) μm (standard deviation of a Gaussian), which results from a diffraction-limited resolution of 3 μm and momentum diffusion of about 3.5 μm of Cs atoms during the 100 μs imaging light pulse. The resolution is separately confirmed by measuring the smallest detectable cloud size for a NaCs BEC.

Microwave system

The setup to generate the microwave dressing fields consists of a cloverleaf antenna array producing a circularly polarized (σ^+) field and two loop antennas, one producing the main linearly polarized (π) microwave field and the other to control the angle between the σ^+ and π fields. The array and the loop antennas are supplied by two separate chains of microwave components, as shown in the block diagrams in Extended Data Fig. 1. The array, described in detail in ref. 68, consists of four resonant loop antennas in a cloverleaf configuration that are fed by a single microwave source. Phase shifts between the loops can be controlled to generate clean circular polarization. The cloverleaf antenna is oriented to emit along the vertical *z* axis, with circular polarization in the *x*–*y* plane. The single-loop antenna producing the main π field is oriented to emit along the horizontal *x* axis, with linear polarization along the *z* axis. The second loop antenna, which emits along the *z* axis, is used to align the polarization vector of the linear π field to the circularly polarized σ^+ field. This is achieved by the careful tuning of the amplitude and phase of the field. The molecules are prepared in the microwave-shielded dressed state by first adiabatically increasing the σ^+ field and then the π field. Each intensity ramp is performed within 40 μs.

In detail, the chains of microwave components are as follows. The σ^+ branch starts with a SG12000 signal generator from DS Instruments. Its output is fed into a voltage-controlled attenuator (General Microwave, D1954) followed by a radiofrequency switch (Mini-Circuits, ZFSWA2R-63DR+). An amplifier (RF Bay, JPA-1000-8000-5) is then used to reach the necessary high power. To reduce the phase noise of the amplifier, responsible for one-body loss of molecules because of transitions to unshielded states, its output is filtered by a 6-MHz-bandwidth cavity (WT Microwave, WT-A10140-Q04). To prevent potential reflections from the cavity that may damage the equipment, we use isolators (Raditek, RADI-3.4-3.6-S3-10WR-10WFWD-H21) on each of its sides. The amplified and filtered signal is then split through a power splitter (Mini-Circuits, ZN4PD1-63-S+) into four different branches, each connected to one of the four antennas of the array. By varying the length of the cable connecting the splitter to each antenna (labelled phase shifters in Extended Data Fig. 1), we realize the relative 90° phase shifts that generate σ^+ polarization. The π branch starts with a second SG12000 signal generator; its output is immediately split into two branches, one with a relative phase shift and attenuation with respect to the other given by a PS6000L phase shifter from DS Instruments. The two branches then follow identical paths mirroring the σ^+ branch, except that the two signals are not split into four but are directly fed into the two loop antennas.

Rabi frequencies, angle between microwaves and ellipticities

To measure the π Rabi frequency, Ω_π, we observe Rabi oscillations between $|0, 0\rangle$ and $|1, 0\rangle$. The σ^+ Rabi frequency, Ω_σ, is determined using dressed-state spectroscopy (S.Z. et al., manuscript in preparation). Owing to the use of narrow-bandwidth cavity filters in the microwave path, the direct measurement of the resonant Rabi frequency is not possible. The probe field for the dressed-state spectroscopy is given by the σ^+ output of the π antenna, which does not produce a perfectly pure linear polarization. To perform dressed-state spectroscopy, we initially increase the σ^+ field to prepare the molecules in the $|+\rangle$ dressed state, using the detuning reported in the main text. Then we abruptly turn on the field produced by the π antenna for a time shorter than a π pulse between the $|+\rangle$ and $|-\rangle$ dressed states. By scanning the frequency of the probe field, we find the centre frequency of the transition, ω, which in turn gives the σ^+ Rabi frequency through the relation $\omega - \omega_0 - \Delta_\sigma = \sqrt{\Omega_\sigma^2 + \Delta_\sigma^2}$, where $\omega_0/2\pi$ is the known $|0, 0\rangle \leftrightarrow |1, 1\rangle$ transition frequency and Δ_σ the known detuning from the same transition.

Imperfections of the π field are quantified in terms of its residual circular polarization. For example, a tilt of the π field will lead to a linearly polarized component in the *x*–*y* plane, which can be decomposed into a σ^+ and a σ^- contribution. We use the second loop antenna, which emits along the *z* axis, to minimize this σ^- component, leaving a residual σ^+-polarized field at the frequency of the π radiation. To measure it, we combine the knowledge of Ω_π with the measurement of Rabi oscillations between the dressed states $|+\rangle$ and $|-\rangle$. Because the only allowed transitions between these states involve a σ^+ photon, the Rabi frequency of the dressed state oscillation, $\Omega_{dressed}$, shows the projection of the π field onto the σ^+ field. Thus, the σ^+ component of the π field is determined by $\arctan(\Omega_{dressed}/(\Omega_\pi \sin^2(\phi)))$. The quantity $\sin^2(\phi)$ accounts for the relative strength of the dressed state sideband transitions (S.Z. et al., manuscript in preparation), with ϕ given by $\sin(2\phi) = 1/\sqrt{1 + (\Delta_\sigma/\Omega_\sigma)^2}$. From these measurements, we determine that the σ^+-polarized component of the π field is about 30% of the main

π component. To ensure the full cancellation of the dipole moment, the size of this circular component of the π field needs to be minimized, setting the limit for how well we can compensate the dipole moment (T.K. et al., manuscript in preparation).

We determine the ellipticity of the σ^+ field through the direct measurement of the relative Rabi frequencies of the σ^- and σ^+ transitions[68]. In our experimental setup, we cannot directly infer the orientation of the ellipticity, which determines the direction of the molecular dipoles.

Cloud fitting

To extract the thermal and condensed components of the molecular gas, we perform bimodal fits to the absorption images. To this end, the absorption images are integrated along the x- and y-directions for better signal-to-noise ratios. The two resulting 1D profiles are simultaneously fitted by the fitting function in direction α ($\alpha = x, y$):

$$n(\alpha) = \frac{15}{16}\frac{N_{\mathrm{TF}}}{\sigma_{\mathrm{TF},\alpha}}\max\left(1-\left(\frac{\alpha-\alpha_{\mathrm{TF}}}{\sigma_{\mathrm{TF},\alpha}}\right)^2, 0\right)^2 + \frac{N_{\mathrm{G}}}{\sqrt{2\pi}\sigma_{\mathrm{G}}}\exp\left(-\frac{(\alpha-\alpha_{\mathrm{G}})^2}{2\sigma_{\mathrm{G}}^2}\right).$$

Along both directions, the molecule number in the thermal cloud, N_{G}, the molecule number in the condensed cloud, N_{TF}, and the Gaussian radius of the thermal cloud, σ_{G}, are kept identical; $\sigma_{\mathrm{TF},\alpha}$ is the Thomas–Fermi radius, α_{TF} is the centre of the condensed cloud and α_{G} is the centre of the thermal cloud in direction α.

Using the results of the fit, the condensate fraction is given by $N_{\mathrm{c}} = N_{\mathrm{TF}}/(N_{\mathrm{G}} + N_{\mathrm{TF}})$ and the peak density is given by $n_0 = [15^{2/5}/(8\pi)][M^3\bar{\omega}^3 N_{\mathrm{c}}/(\hbar^3 a_{\mathrm{s}}^{3/2})]^{2/5}$ (ref. 69), where $\bar{\omega}$ is the geometric mean of the trap frequencies. We note that the calculation of peak density takes into account the effect of s-wave interactions but neglects dipolar interactions. Their inclusion is expected to lead to slightly higher values of the peak densities.

For absorption images obtained at various points of the evaporation sequence, we compare the quality of the bimodal fits with simple Gaussian fits. We find that in the thermal regime, the χ^2 values of the Gaussian and the bimodal fits are nearly identical, whereas in the degenerate regime, the bimodal fit consistently yields a lower χ^2 value. Extended Data Fig. 2 shows the ratio of the χ^2 values of the Gaussian fits and the bimodal fits, with a behaviour similar to that seen in ref. 2.

Condensate lifetime model

We extract the two-body loss rate, $\beta_{2\mathrm{B}}$, of a quasi-pure condensate from a fit of the lifetime data. For the fit, we use the model of ref. 70, which includes one- and two-body contributions to the loss and takes into account bosonic quantum statistics. The differential equation governing the evolution of molecule number as a function of time is

$$\dot{N} = -\beta_{2\mathrm{B}} c_2 N^{7/5} - N/\tau_{1\mathrm{B}},$$

where $\tau_{1\mathrm{B}}$ is the one-body lifetime, $c_2 \equiv [15^{2/5}/(14\pi)]\,[M\bar{\omega}/(\hbar a_{\mathrm{s}})]^{6/5}$, M is the molecular mass and $\bar{\omega}$ is the geometric mean of the trap frequencies. We use the one-body loss rate $\tau_{1\mathrm{B}} = 5.0(2)$ s as a fixed parameter in this fit. The one-body loss rate is independently measured by fitting the loss of a molecular cloud at 700 nK for very long hold times (about 20 s). The one-body loss rate is probably set by off-resonant scattering of the optical trapping light.

Calculation of scattering and dipolar length

We determine the scattering length and dipolar interactions from coupled-channels scattering calculations (T.K. et al., manuscript in preparation). The coupled-channels calculations are similar to those described in refs. 47,71 but extended with a second microwave field with a different frequency and polarization. In essence, the calculations describe two molecules modelled as rigid rotors that interact with each other through dipole–dipole interactions, with a static magnetic field and with two microwave electric fields. The end-over-end rotation of the molecules about each other is described by a partial wave expansion. We then numerically solve the coupled-channels equations subject to an absorbing boundary condition at short range that models collisional loss[47]. By matching to the asymptotic boundary conditions at long range, we obtain a scattering S matrix, from which we determine the elastic and inelastic cross-sections and rate coefficients, and we extract the scattering length a_{s} from the low-energy behaviour of the elastic s-wave element of the S matrix. We determine the dipolar length scale from the same calculation by analysing the long-range interaction between two molecules in the initial state. This numerical calculation essentially describes the time-averaged dipole–dipole interaction between two molecules in eigenstates dressed by the two microwave fields. We equate this interaction to $-2d_{\mathrm{eff}}^2 C_{2,0}(\theta,\phi)/4\pi\epsilon_0 R^3$, which yields an effective dipole moment that sets the dipolar length scale $a_{\mathrm{dd}} = Md_{\mathrm{eff}}^2/(12\pi\hbar^2\epsilon_0)$. Here $C_{2,0}(\theta,\phi)$ is a Racah-normalized spherical harmonic depending on the polar angles of the intermolecular axis with respect to the lab-fixed frame in which the microwave polarizations are defined. By diagonalizing the Hamiltonian excluding the radial kinetic energy, we obtain the adiabatic potential curves shown in Fig. 1d, and the bound states supported by this potential curve are determined by a sinc-DVR calculation[72].

Data availability

The experimental data that support the findings of this study are available from the corresponding author upon reasonable request. Source data are provided with this paper.

Code availability

All relevant codes are available from the corresponding author upon reasonable request.

64. Warner, C. et al. Overlapping Bose-Einstein condensates of ^{23}Na and ^{133}Cs. *Phys. Rev. A* **104**, 033302 (2021).
65. Lam, A. Z. et al. High phase-space density gas of NaCs Feshbach molecules. *Phys. Rev. Res.* **4**, L022019 (2022).
66. Stevenson, I. et al. Ultracold gas of dipolar NaCs ground state molecules. *Phys. Rev. Lett.* **130**, 113022 (2023).
67. Warner, C. et al. Efficient pathway to nacs ground state molecules. *New J. Phys.* **25**, 053036 (2023).
68. Yuan, W. et al. A planar cloverleaf antenna for circularly polarized microwave fields in atomic and molecular physics experiments. *Rev. Sci. Instrum.* **94**, 123201 (2023).
69. Dalfovo, F., Giorgini, S., Pitaevskii, L. P. & Stringari, S. Theory of Bose-Einstein condensation in trapped gases. *Rev. Mod. Phys.* **71**, 463–512 (1999).
70. Söding, J. et al. Three-body decay of a rubidium Bose–Einstein condensate. *Appl. Phys. B* **69**, 257–261 (1999).
71. Karman, T. & Hutson, J. M. Microwave shielding of ultracold polar molecules with imperfectly circular polarization. *Phys. Rev. A* **100**, 052704 (2019).
72. Colbert, D. T. & Miller, W. H. A novel discrete variable representation for quantum mechanical reactive scattering via the *S*-matrix Kohn method. *J. Chem. Phys.* **96**, 1982–1991 (1992).

Acknowledgements We thank C. Greene, A. Elkamshishy and S. Singh for their discussions and preliminary calculations on the field-linked bound states in the shielding potentials, and R. Wooten, T. Yefsah and M. Zwierlein for critical reading and helpful comments on the paper. We are grateful to A. Lam and C. Warner for their contributions to the construction of the experimental apparatus. We also thank I. Bloch, T.-L. Ho and V. Vuletić for their discussions. We acknowledge E. Bellingham and H. Kwak for their experimental assistance. We thank Rohde & Schwarz for the loan of equipment. This work was supported by an NSF CAREER Award (award no. 1848466), an ONR DURIP Award (award no. N00014-21-1-2721), a grant from the Gordon and Betty Moore Foundation (award no. GBMF12340) and a Lenfest Junior Faculty Development Grant from Columbia University. W.Y. acknowledges support from the Croucher Foundation. I.S. was supported by the Ernest Kempton Adams Fund. S.W. acknowledges additional support from the Alfred P. Sloan Foundation.

Author contributions All authors contributed substantially to the work presented in this paper. N.B., W.Y., S.Z. and I.S. carried out the experiments and improved the experimental setup. T.K. performed the theoretical calculations. S.W. supervised the study. N.B., I.S. and S.W. wrote the paper. All authors contributed to the development of the experimental concepts, interpretation of the data and reviewed the paper.

Competing interests The authors declare no competing interests.

Additional information

Supplementary information The online version contains supplementary material available at https://doi.org/10.1038/s41586-024-07492-z.

Correspondence and requests for materials should be addressed to Sebastian Will.

Peer review information *Nature* thanks Lauriane Chomaz, Simon Cornish and the other, anonymous, reviewer(s) for their contribution to the peer review of this work. Peer reviewer reports are available.

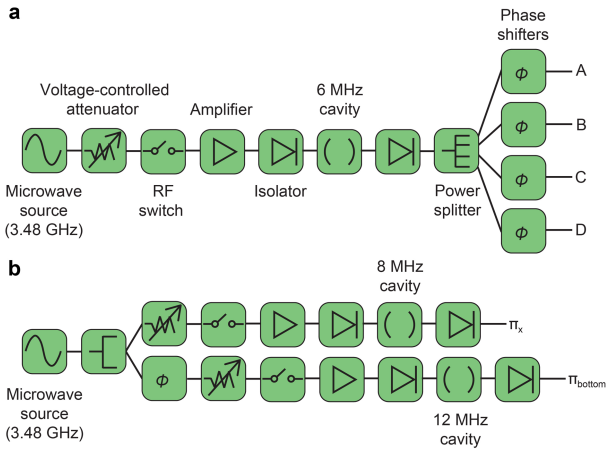

Extended Data Fig. 1 | Microwave setup. a, Block diagram of the microwave components producing the σ^+ field. **b**, Block diagram of the microwave components producing the π field. MHz-level detunings are omitted from the shown frequencies of the source.

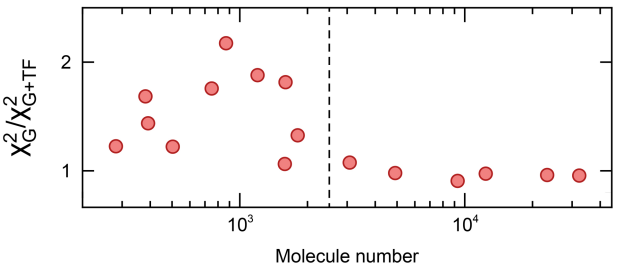

Extended Data Fig. 2 | Comparison of fitting models. Ratio of χ^2-values for Gaussian and bimodal fits. The vertical dashed line marks the onset of the phase transition.